Induction Theorem Analysis of Resonant Nanoparticles: Design of a Huygens Source Nanoparticle Laser

Iñigo Liberal,[1] Iñigo Ederra,[1] Ramón Gonzalo,[1] and Richard W. Ziolkowski[2]
[1]*Electrical and Electronic Engineering Department, Universidad Pública de Navarra, Campus Arrosadía, Pamplona, 31006 Spain*
[2]*Department of Electrical and Computer Engineering, University of Arizona, Tucson, Arizona 85721, USA*
(Received 28 February 2014; published 15 May 2014)

We propose an advanced formulation of standard antenna theory for the basic investigation and design of resonant nanoparticles. This methodology is based on transforming the original scattering problem into a radiation configuration by invoking the induction theorem. Then applying basic antenna theory principles, such as the suppression of any reactive power, the properties of the resonances are engineered. This nanoantenna approach has been validated by revisiting a number of well-known multilayered core-shell structures. It provides additional important physical insights into how the core-shell structures operate and it enables combinations of different resonant phenomena associated with them, e.g., plasmonic and high-ε resonances, in an intuitive manner. Its efficacy is demonstrated by designing a multilayered nanoparticle that achieves lasing with a maximum directivity in the forward direction and a null in the backward direction, i.e., a Huygens source nanoparticle laser.

DOI: 10.1103/PhysRevApplied.1.044002

I. INTRODUCTION

The study of resonant scattering in nanometer-sized entities has been a topic of fundamental interest in multiple disciplines, including astrophysics, atmospheric science, biology, chemistry, electrical engineering, optics, and physics [1]. Furthermore, subwavelength resonators have been essential for the development of metamaterials [2]. More recently, the interest in resonant scattering from nanoparticles has been driven by a technological desire to control light and light-matter interactions at the nanoscale. A variety of physics-driven applications of these resonant nanoparticles have been considered recently, e.g., metactronics (photonic circuits) [3], nanosensors [4,5], thermal emission control [6], and energy harvesting [7].

Plasmonic-based resonant nanoparticles and nanoantennas have probably yielded the most promising designs of subwavelength resonators at infrared and optical frequencies. They enable the concentration, guiding, and enhanced emission of electromagnetic fields with deeply subwavelength sizes [8–13]. Spherical core-shell resonators, i.e., dielectric particles coated with plasmonic shells, are of particular interest. They facilitate the development of subwavelength resonators with tunable resonance frequencies and isotropic responses [14–18]. Inversely, plasmonic coatings also offer the possibility to significantly reduce (cloak, transparency, or jam) the scattering from a nanoparticle [19–23].

In the last few years, Mie resonances in high-ε nanospheres have been rediscovered as a low-loss alternative to plasmonic technology. Available high-ε materials facilitate the application of this paradigm in the terahertz (e.g., $\varepsilon_{TiO_2} \sim 100$ [24]), infrared (e.g., $\varepsilon_{PbTe} \sim 31$ [6,25]), and even optical frequencies (e.g., $\varepsilon_{Si} \sim 15$ [26]). As a matter of fact, the relatively high permittivity of silicon (Si) has enabled the experimental verification of magnetic dipole resonances at optical frequencies [27,28], Fano resonances [29], and highly directive, zero backscattering nanoparticles [30,31] inspired by Kerker's work [32]. Moreover, several reports have demonstrated that the electric [21, 33–39] and magnetic [40] dipole responses of a nanoparticle can be boosted by making use of active materials. Interestingly, the scattering efficiency of these nanoparticles does not monotonically increase along with gain, but there is a threshold value at which the scattering efficiency increases by several orders of magnitude. From a field standpoint, these structures benefit from the concentration of the field intensity in a nanoscopic cavity filled with gain, and they are usually referred to as nanoparticle lasers and/or superresonant structures [34,35,41–48]. Inversely, active materials can also be applied to overcome some of the intrinsic limitations of passive cloaking [49,50].

There have also been numerous discussions on how to achieve higher directivity beyond that available from the electric or magnetic dipole modes. The concept of using the higher order modes from nanoantennas loaded with negative-parameter materials and plasmonic nanoparticles is considered in Refs. [51,52]. Superscattering is considered by employing multiple higher order resonances of nanorods and nanospheres in Refs. [53,54]. By exciting balanced electric and magnetic dipole resonances at the same frequency, there have been numerous reports of unidirectional scattering, e.g., Refs. [6,55]. By introducing a hole in the outer layer of a core-shell particle, which introduces higher order modes, a unidirectional lasing nanoparticle has

been demonstrated [56]. However, because the higher order modes (HOMs) have successively narrower bandwidths and, hence, require more precision in realizing the requisite geometries, any HOM approach will be more susceptible to the issues that plague superdirectivity, which is a well-known ill-posed problem [57]. The simpler dipolar approach has significant advantages in this regard.

In this article, we propose an alternative methodology for the fundamental investigation and design of resonant nanoparticles. The proposed approach is based on transforming the scattering problem into a radiating configuration by invoking the induction theorem (see, e.g., Ref. [58], p. 113 and Ref. [59], p. 333). Following basic antenna theory [57], the design of the resonant nanoparticle can be then carried out by suppressing the reactive power excited in the equivalent radiating problem. This radiation problem viewpoint is transformative for nanoantenna considerations since it transitions their study, which is generally based on scattering concepts, more completely into alignment with standard antenna analysis principles.

This antenna-based approach has been applied to several known resonant scattering nanoparticles and validated (see Supplemental Material [60]). Its utility is exemplified first by using its conceptual advantages to combine plasmonic and high-ε resonant phenomena in an intuitive manner. Its efficacy is then demonstrated by designing a Huygens source nanoparticle laser. Based upon simultaneous electric and magnetic dipole superresonant excitations, this engineered design represents a nanolaser that combines high-directivity and zero-backscattering properties with a giant scattering efficiency. Moreover, the enhanced high directivity is achieved while avoiding the issues associated with the HOM approaches.

Time-harmonic $e^{j\omega t}$ field expressions are assumed and omitted hereafter. All power quantities are written as their time-averaged embodiments. All calculations are performed in MatLab based on the reported analytical expressions.

II. INDUCTION THEOREM

Consider the generic scattering problem depicted in Fig. 1(a). A set of sources $(\mathbf{J}_i, \mathbf{M}_i)$ illuminates a nanoparticle characterized by a certain spatial distribution of permittivity and permeability, $[\varepsilon(\mathbf{r}), \mu(\mathbf{r})]$. The electromagnetic field excited in this problem, $(\mathbf{E}, \mathbf{H})$, can be written as a simple combination of the incident plus scattered fields, i.e., $\mathbf{E} = \mathbf{E}^i + \mathbf{E}^s$ and $\mathbf{H} = \mathbf{H}^i + \mathbf{H}^s$. In this manner, the total field is given by the superposition of the field produced by the sources in the absence of the scatterer, i.e., the incident field, $(\mathbf{E}^i, \mathbf{H}^i)$, plus a field that describes the perturbation introduced by the scatterer, i.e., the scattered field, $(\mathbf{E}^s, \mathbf{H}^s)$. By invoking the induction theorem (Ref. [58], p. 113 and Ref. [59], p. 333), the scattered field exterior to the body can be constructed from the radiation of the equivalent sources $\mathbf{J}_a = -\hat{\mathbf{n}} \times \mathbf{H}^i$, $\mathbf{M}_a = \hat{\mathbf{n}} \times \mathbf{E}^i$ imprinted over the surface of the scatterer [see Fig. 1(b)]. Specifically, the electromagnetic field produced by the sources $(\mathbf{J}_a, \mathbf{M}_a)$ is equal to the scattered field $(\mathbf{E}^s, \mathbf{H}^s)$ exterior to the obstacle, while it is equal to the total field $(\mathbf{E}, \mathbf{H})$ within the obstacle. This formulation emphasizes the scattered field as the radiation arising from a set of sources associated with the scatterer. Moreover, as it is developed later on, it justifies the reciprocity between resonant scattering and the enhanced radiation from localized sources in the presence of material loading observed in a number of numerical studies [14,61]. Furthermore, it enables the design of scattering systems based on antenna engineering related concepts [57].

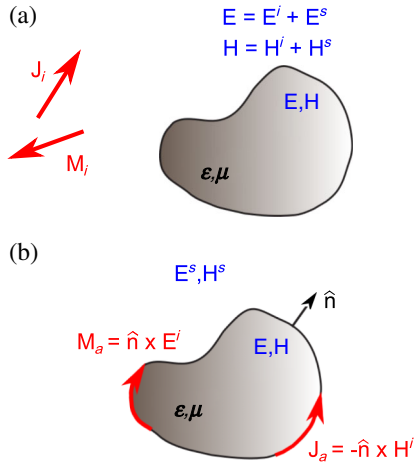

FIG. 1. Sketch of an arbitrary scattering problem (a), and its induction equivalent (b).

To this end, let us analyze the induction equivalent problem separately. In particular, we define the electromagnetic field $(\mathbf{E}^a, \mathbf{H}^a)$, where $(\mathbf{E}^a, \mathbf{H}^a) = (\mathbf{E}^s, \mathbf{H}^s)$ exterior to the scatterer, and $(\mathbf{E}^a, \mathbf{H}^a) = (\mathbf{E}, \mathbf{H})$ interior to the scatterer, produced by the sources $\mathbf{J}_a = -\hat{\mathbf{n}} \times \mathbf{H}^i$ and $\mathbf{M}_a = \hat{\mathbf{n}} \times \mathbf{E}^i$. This set of fields $(\mathbf{E}^a, \mathbf{H}^a)$ and sources $(\mathbf{J}_a, \mathbf{M}_a)$ satisfies Maxwell's equations in the presence of the obstacle (scatterer). The complex Poynting's theorem associated with this system of equations can be stated as

$$
\begin{aligned}
-\frac{1}{2}\iiint_V [\mathbf{E}^a \cdot \mathbf{J}_a^* + \mathbf{M}_a \cdot (\mathbf{H}^a)^*] dV \\
= \frac{1}{2}\oiint_{\partial V} \{\mathbf{E}^a \times (\mathbf{H}^a)^*\} \cdot d\mathbf{S} \\
+ 2j\omega \iiint_V \left[\frac{\mu}{4}|\mathbf{H}^a|^2 - \frac{\varepsilon^*}{4}|\mathbf{E}^a|^2\right] dV. \qquad (1)
\end{aligned}
$$

The real part of Eq. (1) represents the conservation of the time-averaged total power in its integral form. Analogously, the imaginary part is the conservation of the time-averaged reactive power. The latter is associated with flows of energy which, although nonzero at specific times, vanish when time averaged. Thus, it does not

contribute to the real net total power. Note that while the real powers must be positive semidefinite for a passive scatterer, the sign of the reactive power reflects the phase shift between the projections of the fields onto the current densities in the left-hand side of (1). Therefore, it can be either positive or negative.

To achieve a high radiation efficiency, the design of a radiating system requires a complete suppression of the reactive power, i.e., if the reactive power is nonzero, it leads to a mismatch between the feeding network and the radiator, as well as to out-of-phase interactions between the fields and the currents, which in turn leads to an inefficient excitation of the currents on the radiator and coupling of the resulting accepted power into radiated fields. The net result is an inefficient radiator [61–63]. The zeroing out of the total reactive power is of paramount importance in the design of any small radiating system, where it is typically much larger than the total radiated power. In view of the analogy of radiating systems offered by the induction theorem, we propose to follow this philosophy of suppressing the reactive power in the design of resonant nanoparticles.

In the present study, the reactive power is determined by taking the volume of integration V to be the whole space. It follows that the real part of the surface integration in (1) corresponds to the scattered power, while its imaginary part simply vanishes, i.e.,

$$P_{\text{scat}} = \frac{1}{2}\oiint_{\partial V} \text{Re}\{\mathbf{E}^a \times (\mathbf{H}^a)^*\} \cdot d\mathbf{S}, \tag{2}$$

$$\frac{1}{2}\oiint_{\partial V} \text{Im}\{\mathbf{E}^a \times (\mathbf{H}^a)^*\} \cdot d\mathbf{S} = 0. \tag{3}$$

Thus, the reactive power can be computed by means of the imaginary part of the volume integral in the right-hand side of (1), leading to

$$P_{\text{reac}} = 2\omega(W_H - W_E), \tag{4}$$

where

$$W_E = \frac{\varepsilon'}{4}\iiint_V |\mathbf{E}^a|^2 dV, \quad W_H = \frac{\mu'}{4}\iiint_V |\mathbf{H}^a|^2 dV. \tag{5}$$

Equation (4) links the reactive power supplied by the sources to the distribution of electric and magnetic field intensities, weighted by the real part of the medium's constitutive parameters.

At this point, it is worth remarking that the quantities in Eq. (5) do not correspond in general to the net energy stored in the electric and magnetic fields. As far as such quantities are concerned, they should be directly linked to the work done to establish the field from an initial value of zero [64] and/or to the power supplied to the polarization current densities composing the continuous media [65]. Even though additional energy densities in the form $U_E = \frac{1}{4}\partial_\omega\{\omega\varepsilon\}|\mathbf{E}|^2$ and $U_H = \frac{1}{4}\partial_\omega\{\omega\mu\}|\mathbf{H}|^2$ have been derived for fields in lossless media that evolve slowly from their initial zero values [64–66], to the best knowledge of the authors, there is no undisputed formulation of the electromagnetic energy in time-harmonic form for lossy media. Nevertheless, a certain degree of losses must always be present for any dispersive causal material [66].

To overcome this quandary, we will refer to the terms $2\omega W_H$ and $2\omega W_E$ as the power components that describe how the reactive power supplied by the sources is constructed from the contributions associated with the distributions of the magnetic and electric field intensities, respectively. Therefore, $2\omega W_H$ and $2\omega W_E$ can be either positive or negative; and they are not subjected to Foster's theorem [67,68]. Under this perspective, it will be shown that the power density terms $2\omega W_H$ and $2\omega W_E$ are very useful tools to facilitate the design of resonant nanoparticles by balancing the contributions to them from different material regions.

For illustrative purposes, the plots of the scattered and reactive powers will be normalized to the incident power density S_i projected over the physical (geometrical) area of the nanoparticle: A_{geom}. This puts these normalized powers in direct correspondence with the concept of a scattering efficiency [1], whose definition is extended here for the reactive power:

$$Q_{\text{scat}} = \frac{P_{\text{scat}}}{S_i A_{\text{geom}}}, \qquad Q_{\text{reac}} = \frac{P_{\text{reac}}}{S_i A_{\text{geom}}}. \tag{6}$$

III. ANALYTICAL FORMULATION FOR MULTILAYERED SPHERICAL PARTICLES

The recent analysis [69] introduces a closed-form formulation for evaluating W_H and W_E in a lossless, single layer spherical problem to calculate the reactive power in a canonical configuration associated with understanding the physics of the fundamental limit of the quality factor Q of an antenna. The analytical formulation introduced below allows one to compute W_H and W_E, again in closed form, for a lossy scatterer represented by the multilayered sphere shown in Fig. 2. As will be demonstrated, the resulting expressions significantly enhance our abilities to understand the underlying physics of resonant nanoparticles.

As schematically depicted in Fig. 2, the scattering problem configuration consists of the whole space being divided into a number of concentric spherical layers. The last layer extends from the spherical surface that circumscribes the multilayered particle to infinity. Therefore, if there are $N+1$ regions, there are N spherical interfaces separating them defined by their radii: $r_1, r_2, \ldots, r_N$. In any of these layers, the electromagnetic field can be written in terms of the Stratton vector fields as [58–60]

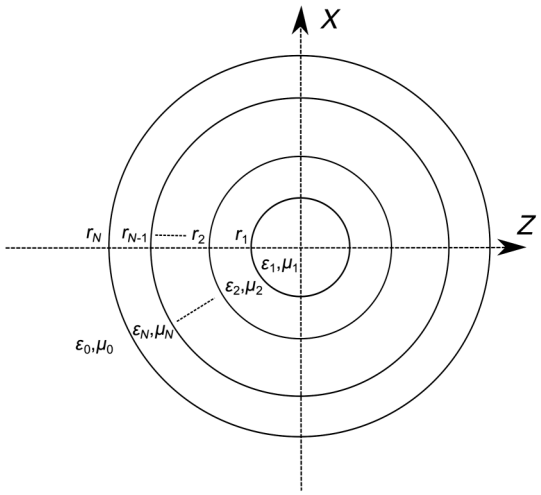

FIG. 2. Depiction of a spherical body consisting of N concentric layers with external radii ranging from r_1 to r_N.

$$\mathbf{E}^a = -\sum_{\{q\}}\{jc^{\mathrm{TM}}_{\{q\}}\mathbf{N}^{<}_{\{q\}}(kr) + jd^{\mathrm{TM}}_{\{q\}}\mathbf{N}^{>}_{\{q\}}(kr) + c^{\mathrm{TE}}_{\{q\}}\mathbf{M}^{<}_{\{q\}}(kr) + d^{\mathrm{TE}}_{\{q\}}\mathbf{M}^{>}_{\{q\}}(kr)\}, \tag{7}$$

$$\mathbf{H}^a = \frac{1}{\eta}\sum_{\{q\}}\{c^{\mathrm{TM}}_{\{q\}}\mathbf{M}^{<}_{\{q\}}(kr) + d^{\mathrm{TM}}_{\{q\}}\mathbf{M}^{>}_{\{q\}}(kr) - jc^{\mathrm{TE}}_{\{q\}}\mathbf{N}^{<}_{\{q\}}(kr) - jd^{\mathrm{TE}}_{\{q\}}\mathbf{N}^{>}_{\{q\}}(kr)\}, \tag{8}$$

where k and η are the propagation constant and wave impedance of the medium in a given layer, respectively, and $\mathbf{N}^{<}_{\{q\}}(kr)$ and $\mathbf{M}^{<}_{\{q\}}(kr)$ are the Stratton vector fields [60]. The symbol $\{q\} = \{n, m, l\}$, is a multiindex introduced to simplify the notation. In particular, the summation over $\{q\}$ runs over all TM or TE multipoles $\sum_{\{q\}} = \sum_{n=1}^{\infty}\sum_{m=0}^{n}\sum_{l=e,o}$. The set $\{c^{\mathrm{TM}}_{\{q\}}, d^{\mathrm{TM}}_{\{q\}}, c^{\mathrm{TE}}_{\{q\}}, d^{\mathrm{TE}}_{\{q\}}\}$ represents the multipolar coefficients of the fields with electric field units that must be determined by setting a particular excitation and solving the corresponding boundary value problem. In the most internal layer, i.e., the core ranging from $r = 0$ to $r = r_1$, the coefficients satisfy $d^{\mathrm{TM}}_{\{q\}}, d^{\mathrm{TE}}_{\{q\}} = 0$. Exterior to the scatterer, the coefficients satisfy $c^{\mathrm{TM}}_{\{q\}}$, $c^{\mathrm{TE}}_{\{q\}} = 0$, and, consequently, the corresponding fields represent outgoing waves which are propagating away from the radiating system.

Because of the orthogonality of the spherical harmonics [58–60], it is possible to construct the quantities P_{reac}, W_H, and W_E by superimposing the contribution from each multipole, i.e.,

$$P_{\mathrm{reac}} = \sum_{\{q\}}[P^{\{q\},\mathrm{TM}}_{\mathrm{reac}} + P^{\{q\},\mathrm{TE}}_{\mathrm{reac}}], \tag{9}$$

$$W_H = \sum_{\{q\}}[W^{\{q\},\mathrm{TM}}_{H} + W^{\{q\},\mathrm{TE}}_{H}], \tag{10}$$

$$W_E = \sum_{\{q\}}[W^{\{q\},\mathrm{TM}}_{E} + W^{\{q\},\mathrm{TE}}_{E}], \tag{11}$$

where

$$P^{\{q\},\mathrm{TZ}}_{\mathrm{reac}} = 2\omega(W^{\{q\},\mathrm{TZ}}_{H} - W^{\{q\},\mathrm{TZ}}_{E}) \tag{12}$$

for TZ = TM, TE. As derived in the Supplemental Material [60], the terms $W^{\{q\},\mathrm{TM}}_{E}$, $W^{\{q\},\mathrm{TM}}_{E}$, $W^{\{q\},\mathrm{TM}}_{H}$, and $W^{\{q\},\mathrm{TM}}_{H}$ in a spherical layer defined between the radial coordinates r_{in} and r_{out} can be analytically evaluated in closed form as follows:

$$W^{\{q\},\mathrm{TM}}_{H} = \frac{\mu'}{4|\eta|^2}\frac{f_{nm}}{k_0^2}\{|c^{\mathrm{TM}}_{\{q\}}|^2\xi_{JJ}(kr) + |d^{\mathrm{TM}}_{\{q\}}|^2\xi_{HH}(kr) + 2\mathrm{Re}[d^{\mathrm{TM}}_{\{q\}}(c^{\mathrm{TM}}_{\{q\}})^*\xi_{JH}(kr)]\}^{r_{\mathrm{out}}}_{r_{\mathrm{in}}}, \tag{13}$$

$$W^{\{q\},\mathrm{TE}}_{H} = \frac{\mu'}{4|\eta|^2}\frac{f_{nm}}{k_0^2}\{|c^{\mathrm{TE}}_{\{q\}}|^2\varphi_{JJ}(kr) + |d^{\mathrm{TE}}_{\{q\}}|^2\varphi_{HH}(kr) + 2\mathrm{Re}[d^{\mathrm{TE}}_{\{q\}}(c^{\mathrm{TE}}_{\{q\}})^*\varphi_{HJ}(kr)]\}^{r_{\mathrm{out}}}_{r_{\mathrm{in}}}, \tag{14}$$

$$W^{\{q\},\mathrm{TM}}_{E} = \frac{\varepsilon'}{4}\frac{f_{nm}}{k_0^2}\{|c^{\mathrm{TM}}_{\{q\}}|^2\varphi_{JJ}(kr) + |d^{\mathrm{TM}}_{\{q\}}|^2\varphi_{HH}(kr) + 2\mathrm{Re}[d^{\mathrm{TM}}_{\{q\}}(c^{\mathrm{TM}}_{\{q\}})^*\varphi_{HJ}(kr)]\}, \tag{15}$$

$$W^{\{q\},\mathrm{TE}}_{E} = \frac{\varepsilon'}{4}\frac{f_{nm}}{k_0^2}\{|c^{\mathrm{TE}}_{\{q\}}|^2\xi_{JJ}(kr) + |d^{\mathrm{TE}}_{\{q\}}|^2\xi_{HH}(kr) + 2\mathrm{Re}[d^{\mathrm{TE}}_{\{q\}}(c^{\mathrm{TE}}_{\{q\}})^*\xi_{JH}(kr)]\}^{r_{\mathrm{out}}}_{r_{\mathrm{in}}}, \tag{16}$$

where $f_{nm} \in \mathbb{R}^+$ is an auxiliary constant defined as

$$f_{nm} = (1 + \delta_{m0})\frac{2\pi n(n+1)}{2n+1}\frac{(n+m)!}{(n-m)!}, \tag{17}$$

while $\xi_{FG}(kr)$ and $\varphi_{FG}(kr)$ are real-valued functions defined as

$$\xi_{FG}(kr) = \frac{1}{k^2 - (k^*)^2}\{k^*\hat{F}_n(kr)[\hat{G}_{n-1}(kr)]^* - k\hat{F}_{n-1}(kr)[\hat{G}_n(kr)]^*\}, \tag{18}$$

$$\varphi_{FG}(kr) = \frac{1}{k^2 - (k^*)^2}\{k\hat{F}_n(kr)[\hat{G}'_n(kr)]^* - k^*\hat{F}'_n(kr)[\hat{G}_n(kr)]^*\}. \quad (19)$$

The terms $\hat{F}_n(z)$ and $\hat{G}_n(z)$ are linear combinations of the Schelkunoff functions [58–60]: $\hat{J}_n(z)$ and $\hat{Y}_n(z)$, and their derivatives. Their coefficients are independent of n and z. The term $\xi_{JG}(kr)$ represents the evaluation of $\xi_{FG}(kr)$ with $\hat{F}_n(z) = \hat{J}_n(z)$, $\varphi_{FH}(kr)$ represents the evaluation of $\varphi_{FG}(kr)$ with $\hat{G}_n(z) = \hat{H}_n^{(2)}(z)$, and so on.

Equations (13)–(16) are an important contribution from this article. They enable the evaluation of W_E and W_H in an analytical closed form (with virtually no computational burden) for lossy multilayered scatterers, and thus assist in the design of radiating and resonant scattering systems. They can also be adopted to a more generalized study of quality factors than reported in [69] and of the fundamental limits of radiating and resonant scattering systems [70]. Both possibilities are left for future efforts. To finalize, although (13)–(16) are relatively complex expressions, they provide a simpler formulation and starting point that facilitate the asymptotic analyses of electrically small and electrically large scatterers.

We note that both the numerator and denominator of Eqs. (18)–(19) tend to zero when the propagation constant is a real number, i.e., $k \in \mathbb{R}$, which occurs for an ideal lossless media supporting propagating fields. In such a case, one can manipulate Eqs. (18)–(19) to solve the indeterminacy that arises in the computation of the reactive power exterior to the scatterer. The following limit is then applicable and can be derived by manipulating the relationships introduced in [71]

$$\lim_{k\to k_0}\{\varphi_{HH}(kr) - \xi_{HH}(kr)\} = \frac{1}{k_0}\{\hat{J}_n(k_0r)\hat{J}'_n(k_0r) + \hat{Y}_n(k_0r)\hat{Y}'_n(k_0r)\}. \quad (20)$$

It can be readily checked that the limit (20) vanishes as $r \to \infty$. Consequently, the contributions to the reactive power from the exterior of the scatterer can be written simply as

$$P_{\text{reac}}^{\{q\},\text{TZ}} = \pm P_{\text{scat}}^{\{q\},\text{TZ}}\{\hat{J}_n(k_0r_N)\hat{J}'_n(k_0r_N) + \hat{Y}_n(k_0r_N)\hat{Y}'_n(k_0r_N)\}, \quad (21)$$

where the plus sign is chosen for the TM modes and the minus sign for the TE modes. The term $P_{\text{scat}}^{\{q\},\text{TZ}}$ represents the contribution from each spherical multipole to the total scattered power, $P_{\text{scat}} = \sum_{\{q\},\text{TZ}} P_{\text{scat}}^{\{q\},\text{TZ}}$, which can be computed [72] in closed form via the surface integration in (2) as

$$P_{\text{scat}}^{\{q\},\text{TZ}} = \frac{1}{2}\frac{f_{nm}}{\eta_0 k_0^2}|d_{\{q\}}^{\text{TZ}}|^2. \quad (22)$$

IV. CANONICAL EXAMPLE: REVISITING CORE-SHELL RESONATORS

The analogy between resonant nanoparticles and antenna systems inspired by the induction theorem provides a new perspective on their resonant phenomena. For example, resonant plasmonic nanoparticles can be seen as an inductive contribution ($2\omega W_E < 0$) which is facilitated by their negative permittivity at optical frequencies. This material inductive contribution can be used to compensate for the natural capacitance of the electric dipole mode, which is associated with the reactive field external to the particle. Inversely, magnetic dipole resonances in high-ε nanoparticles, which make use of capacitive contributions associated with the electric field being stored within the high-ε material, can compensate for the natural inductive contribution to the reactance arising from the magnetic dipole fields.

To illustrate these concepts further, we analyze here a canonical example consisting of an electrically small

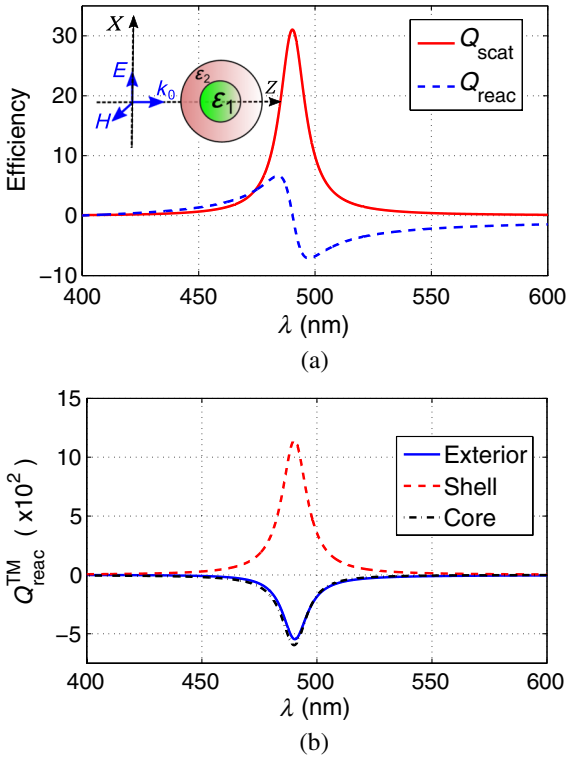

FIG. 3. (a) Scattering and reactive power efficiencies for the TM^{e11} (electric dipole) mode excited by a core-shell nanoparticle with internal $r_1 = 24$ nm and external radii $r_2 = 30$ nm, core relative permittivity $\varepsilon_1 = 3 - j \times 10^{-5}$, and shell permittivity given by the low loss, dispersive Drude model with $\omega_p = 1.39 \times 10^{16}$ rad/s and $\omega_c = \omega_p/1000$. Inset: Geometry and corresponding coordinate system. (b) Contributions to the reactive efficiency from the core, shell, and exterior to the nanoparticle regions.

core-shell resonator. (Additional examples of analyzing canonical structures by means of the induction theorem, such as plasmonic and high-ε nanospheres, are included in the Supplemental Material [60].) Traditionally, the resonances excited in core-shell structures are explained in terms of the excitation of material polaritons on the surface of the scatterer, and mathematically justified by means of Mie theory [1,14,15]. It is found here that they can be explained more physically in terms of their suppression of the reactive power. Our core-shell structure consists of a dielectric core covered with a plasmonic shell as schematically depicted in the inset of Fig. 3(a). It is characterized by internal radius $r_1 = 24$ nm and external radius $r_2 = 30$ nm, core relative permittivity $\varepsilon_1 = 3 - j\times 10^{-5}$, and shell permittivity given by a low loss, dispersive Drude model: $\varepsilon(\omega) = \varepsilon_0\{1 - \omega_p^2/[\omega(\omega - j\omega_c)]\}$ with $\omega_p = 1.39 \times 10^{16}$ rad/s and $\omega_c = \omega_p/1000$.

Figure 3(a) depicts the scattering and reactive power efficiencies, Q_{scat} and Q_{reac}, respectively, for the dominant TM^{e11} (electric dipole) mode excited in this electrically small, core-shell resonator. Consistently, the reactive power is zero at the frequency of the core-shell resonance. Moreover, being a electrically small dielectric particle, the reactive power is dominated by the contribution from the electric field, and the suppression of the reactive power must be produced by opposing contributions from the different layers. As shown in Fig. 3(b), the plasmonic layer compensates for the contributions from both the exterior and core regions of the nanoparticle. Similarly, the fact that P_{reac} is mostly dominated by $2\omega W_E$ can be checked readily by examining the contribution from each different layer, subdivided into both the $2\omega W_E$ and $2\omega W_H$ contributions, as it is depicted in Fig. 4.

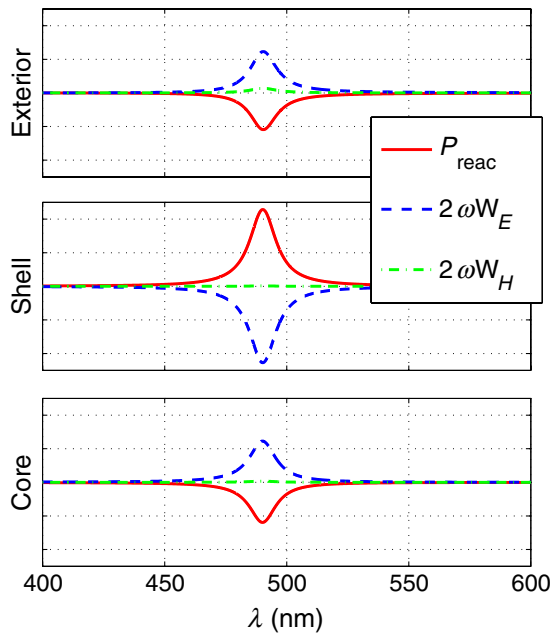

FIG. 4. Contributions to P_{reac}, $2\omega W_E$, and $2\omega W_H$ (in arbitrary units) from the core, shell and exterior regions of the core-shell nanoparticle for the TM^{e11} (electric dipole) mode excited in the core-shell resonator. The core-shell geometry is defined by its internal $r_1 = 24$ nm and external $r_2 = 30$ nm radii, core relative permittivity $\varepsilon_1 = 3 - j \times 10^{-5}$, and shell permittivity given by the low loss, dispersive Drude model with $\omega_p = 1.39 \times 10^{16}$ rad/s and $\omega_c = \omega_p/1000$.

Under this perspective, the design of electrically small core-shell resonators is analogous to the design of electrically small dipole antennas. In essence, the dominant capacitive contribution arising from the reactive electric dipole fields must be tuned with an inductance (the plasmonic shell) to enforce the antenna resonance. At this point, one can also identify a certain parallelism with the circuit model for nanospheres introduced by Engheta *et al.* [73]. However, the present formalism is not restricted to the quasistatic regime. It includes both absorption and radiation losses, and it can be adapted to arbitrarily complex geometries.

V. ENGINEERED RESONANCES WITH COMBINED PLASMONIC AND HIGH-ε LAYERS

The physical insights into resonant phenomena provided by the induction theorem yield more flexibility in tailoring the response of a nanoparticle. This same strategy can be adopted, for example, to combine plasmonic and high-ε resonances. In particular, we introduce a plasmonic layer to tune the electric and magnetic dipole resonances excited in a high-ε nanoparticle. The resulting three layer dielectric sphere is depicted schematically in Fig. 5 with ε_1, ε_2, and ε_3 being the permittivities of those layers and r_1, r_2, and r_3 being their external radii. We set the internal and external permittivities to be equal only to simplify the discussion, i.e., $\varepsilon_1 = \varepsilon_3$. This allows us to understand the structure as a dielectric sphere containing an internal plasmonic layer of thickness t whose central radius $r_c = (r_1 + r_2)/2$ can be used to write $r_1 = r_c - t/2$ and $r_2 = r_c + t/2$.

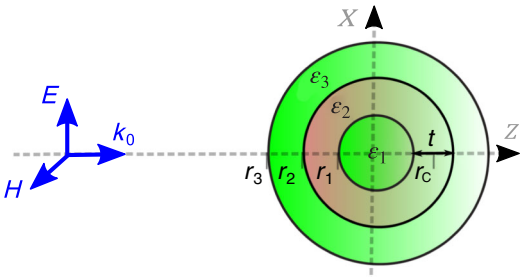

FIG. 5. Sketch of a three-layer sphere with ε_1, ε_2, and ε_3 being the permittivities of its layers and with r_1, r_2, and r_3 being their external radii. This particle is illuminated by a linearly polarized plane wave propagating along $+\hat{\mathbf{z}}$ with the electric field oriented along $\hat{\mathbf{x}}$.

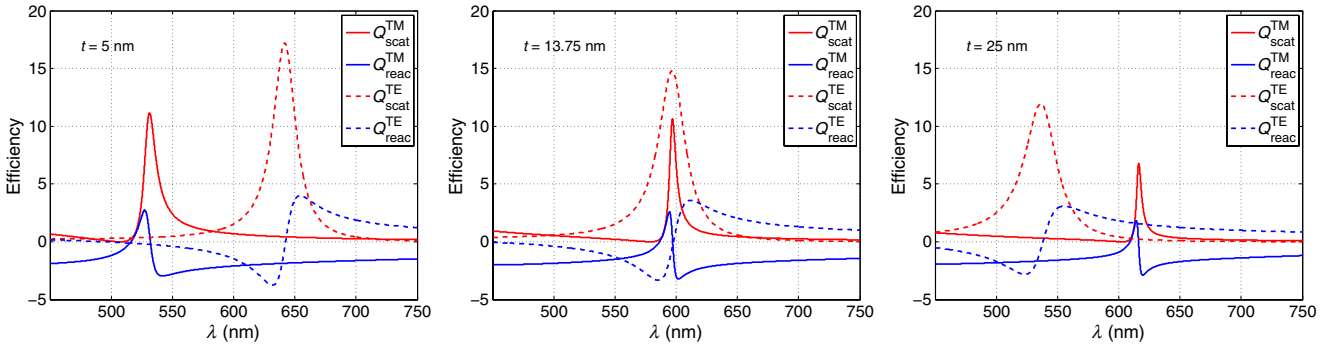

FIG. 6. Scattering and reactive power efficiencies for the TM^{e11} (electric dipole) and TE^{o11} (magnetic dipole) modes for a dielectric nanosphere with an external radius $r_3 = 60$ nm and whose internal plasmonic concentric layer has a central radius $r_c = 30$ nm and a thickness (a) $t = 5$ nm, (b) $t = 13.75$ nm, (c) $t = 25$ nm. The dielectric permittivity of the core and third layer is $\varepsilon_1 = \varepsilon_3 = 30 - j \times 10^{-5}$, and the permittivity of the plasmonic layer ε_2 is characterized by a low loss, dispersive Drude model with $\omega_p = 1.39 \times 10^{16}$ rad/s and $\omega_c = \omega_p/1000$.

The inclusion of the plasmonic layer results in a negative $2\omega W_E$, which in turns reduces the overall contribution to $2\omega W_E$ from within the sphere. The plasmonic layer thus provides an effect opposite to the large positive permittivity, i.e., it shifts the TE^{o11} (magnetic dipole) resonance towards higher frequencies. Inversely, the TM^{e11} (electric dipole) resonance benefits from the inductive contribution of the plasmonic layer, and this resonance is shifted towards lower frequencies. With both resonances moving in opposite directions, they can be readily superimposed. Intuitively, the impact of the plasmonic layer is larger when it is thicker. Consequently, as this thickness increases, both resonances can overlap eventually and even exchange their frequency ordering. In this manner, the use of a plasmonic layer in this spherical configuration enables us to superimpose and/or exchange the frequency ordering of the electric and magnetic resonances excited by a high-ε sphere.

This behavior is illustrated in Fig. 6, which depicts the scattering and reactive power efficiencies for a dielectric nanosphere with an external radius $r_3 = 60$ nm and a concentric internal plasmonic layer whose central radius $r_c = 30$ nm, by varying the thickness of the plasmonic layer: (a) $t = 5$ nm, (b) $t = 13.75$ nm, (c) $t = 25$ nm. The dielectric permittivity of the core (first layer) and the third layer is set at $\varepsilon_1 = \varepsilon_3 = 30 - j \times 10^{-5}$. The permittivity ε_2 of the plasmonic layer is characterized by a low loss, dispersive Drude model with $\omega_p = 1.39 \times 10^{16}$ rad/s and $\omega_c = \omega_p/1000$. These results verify the anticipated shifts in the location of the resonances and illustrate the realizable complete overlap of the electric and magnetic dipole resonances.

Additional information on the impact of the plasmonic layer can be obtained by inspecting the field distributions within the particle. Figure 7 depicts the normalized (with respect to the amplitudes of the incident field) electric and magnetic field intensity distributions on the XZ plane for the TM^{e11} (electric dipole) and TE^{o11} (magnetic dipole) modes. It is apparent from the figure that the spatial distributions of the electric and magnetic field intensities for the TM^{e11} and TE^{o11} modes are complementary. Specifically, the TE^{o11} (magnetic dipole) mode is characterized by an electric field minimum and a magnetic field maximum at the particle center. On the other hand, the opposite features are observed in the TM^{e11} (electric dipole) mode. Therefore, when a thin plasmonic layer is

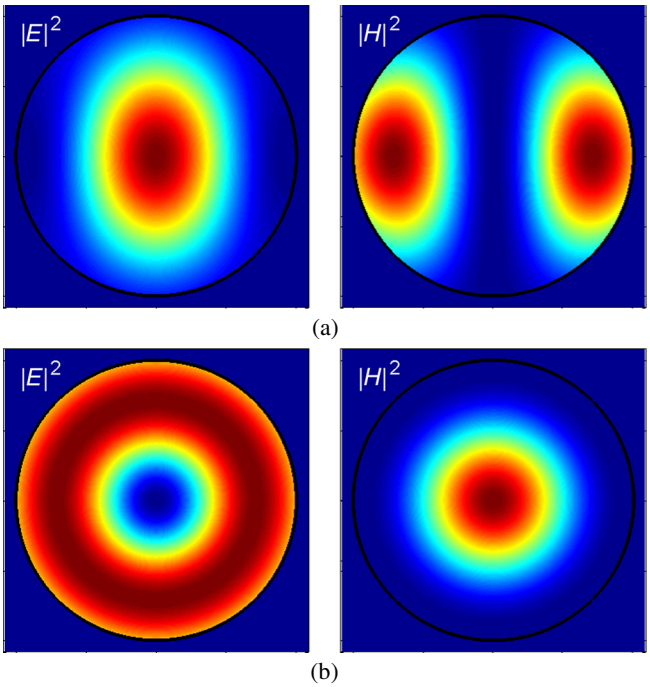

FIG. 7. Electric and magnetic field intensity distributions within the three layer nanoparticle in the XZ plane (normalized to their maximum values) for the (a) TM^{e11} (electric dipole) and (b) TE^{o11} (magnetic dipole) modes.

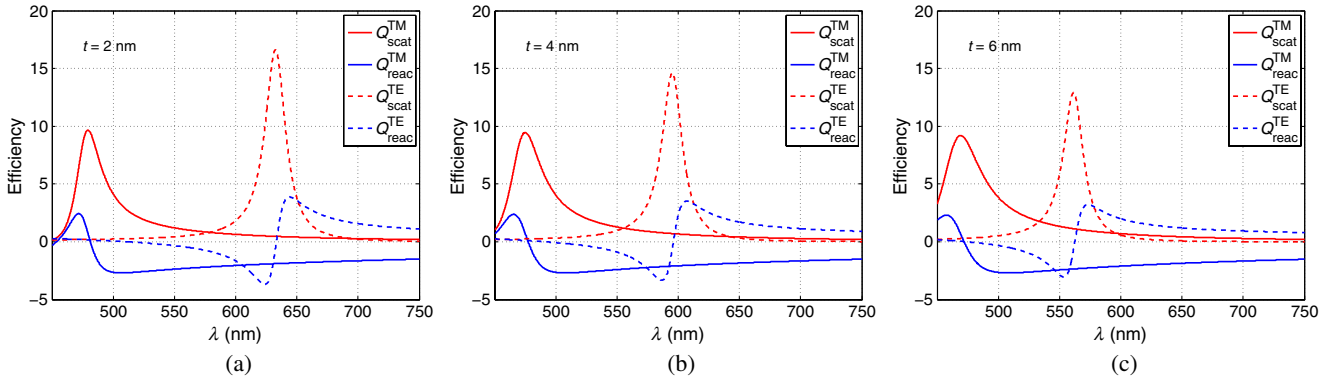

FIG. 8. Scattering and reactive power efficiencies for the TM^{e11} (electric dipole) and TE^{o11} (magnetic dipole mode) for a dielectric nanosphere whose external radius $r_3 = 60$ nm. It has a concentric internal plasmonic layer whose central radius $r_c = 50$ nm. The thickness of this plasmonic layer is varied as (a) $t = 2$ nm, (b) $t = 4$ nm, and (c) $t = 6$ nm. The dielectric permittivity of the first and third layers is $\varepsilon_1 = \varepsilon_3 = 30 - j \times 10^{-5}$; the permittivity of the plasmonic layer ε_2 is characterized by a low loss, dispersive Drude model with $\omega_p = 1.39 \times 10^{16}$ rad/s and $\omega_c = \omega_p/1000$.

placed in the outer part of the particle, it is found that it should mostly affect the TE^{o11} (magnetic dipole) resonance. In contrast, when the plasmonic layer is placed close to the center of the particle, it should mostly affect the TM^{e11} (electric dipole) resonance.

This spatial complementarity of the field intensities allows us to tune independently the electric and magnetic dipole resonances. This effect is evidenced in Fig. 8, which depicts the scattering and reactive power efficiencies when the central radius of the plasmonic layer is set at $r_c = 50$ nm, and its thickness is varied as $t = 2$ nm, $t = 4$ nm, and $t = 6$ nm. This figure corroborates the observation that the magnetic dipole resonance is affected by the plasmonic layer when it is placed toward the outer part of the nanoparticle, where it strongly perturbs the electric field distribution associated with the magnetic dipole mode, and that this placement has a negligible impact on the electric dipole mode, which is characterized by a large, uniform electric field distribution in the core.

VI. HUYGENS SOURCE NANOPARTICLE LASER

The induction theorem-based methodology can be extended further. We apply it to design a Huygens source nanoparticle laser, i.e., a nanolaser that radiates primarily into one hemisphere. The proposed nanoparticle has the same three layer spherical body shown in Fig. 5, but it now consists of a silicon (Si) sphere with an internal silver (Ag) layer. This geometry benefits from a perfect spherical symmetry, which results in an isotropic behavior, i.e., directional scattering is obtained independent of the direction of arrival of the incident field and this enhanced response propagates in that same direction.

As in [34], the permittivity of the Ag nanolayer is taken to be $\varepsilon_{Ag}(\omega, t) = \varepsilon_{Drude}(\omega, t) + \chi_{intband}(\omega)$, where $\varepsilon_{Drude}(\omega, t)$ is a thickness-dependent Drude model and $\chi_{intband}(\omega)$ describes the responses of the interband transitions. The Si dielectric layers are modeled with the refractive index $n_{Si} = 3.5$ (see, e.g., Ref. [26]). Following the procedure presented in Sec. V, it is possible to superimpose simultaneously both the TM^{e11} (electric dipole) and TE^{o11} (electric dipole) resonances at the same frequency. For example, both resonances coincide at $\lambda = 700$ nm for $r_c = 74.5$ nm, $t = 15$ nm, $r_3 = 120$ nm, as illustrated in the top left figure of the panel shown in Fig. 9.

To overcome the losses associated with the plasmonic layer, we next introduce gain uniformly into the dielectric layers and study the response of the resulting active nanoparticle. The refractive index of Si is assumed to have a canonical imaginary part κ, or, equivalently, the permittivity of Si is taken to be $\varepsilon_{Si} = n_{Si}^2 - \kappa^2 + j2n_{Si}\kappa$. In practice, the gain could be realized, for instance, by incorporating quantum dots into the Si layers or by doping these semiconductor layers.

In order to guide the design process, we note that the previously mentioned complementarity in the field distributions of the TM^{e11} (electric dipole) and TE^{o11} (magnetic dipole) modes for the passive nanoparticle (see Fig. 7), suggests that the electric and magnetic dipole superresonance states could be tuned almost independently by modifying the gain parameters independently in the inner (κ_1) and outer (κ_2) Si layers. The resulting overlap of both dipole modes enables the design of an active Huygens source nanoparticle. Specifically, the complementarity in the field distributions implies that increasing the gain in the internal Si layer mostly benefits the TM^{e11} (electric dipole) resonance. This intuition is verified in Fig. 9, which represents the scattering efficiency Q_{scat} and the contributions to it from the electric and magnetic dipole modes, Q^e_{scat} and Q^m_{scat}, respectively. The external radius of the nanoparticle is $r_3 = 120$ nm. The outer Si layer is taken to be passive with $\kappa_2 = 0$. The concentric internal Ag layer has a central radius $r_c = 74.5$ nm and a thickness $t = 15$ nm. The κ_1 values in the inner Si layer (the core) are

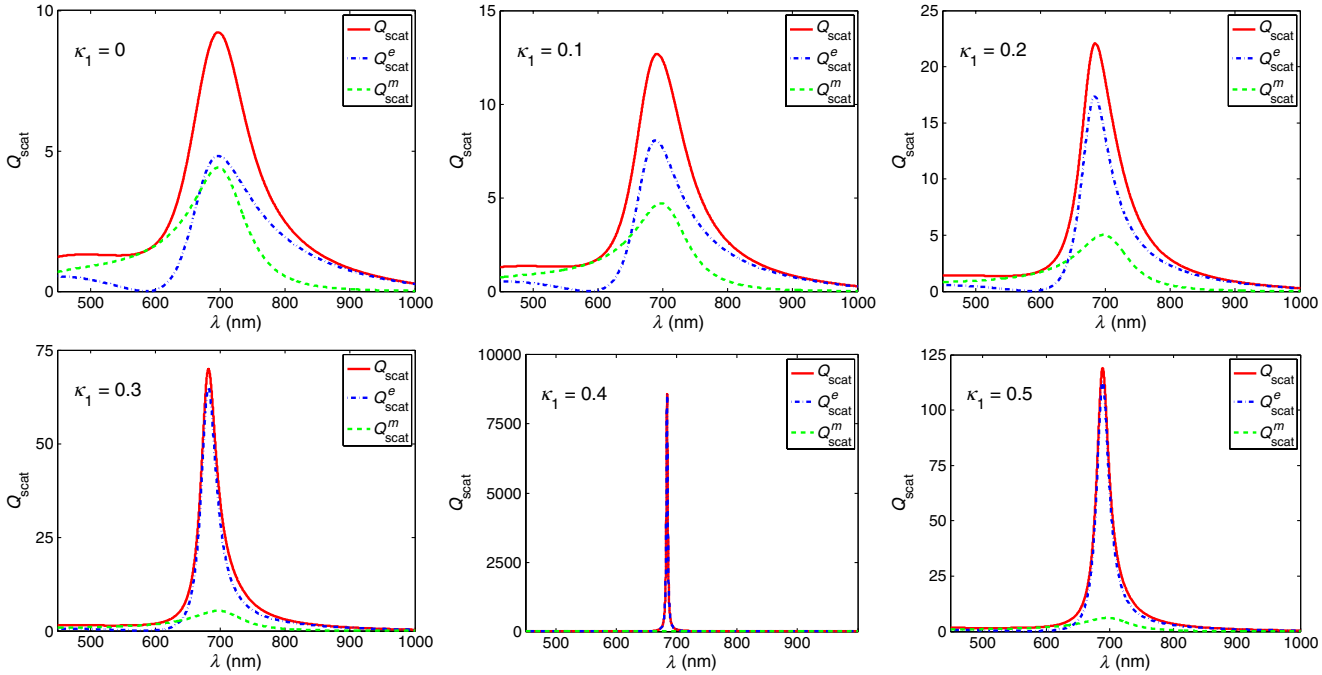

FIG. 9. Scattering efficiencies Q_{scat} and the contributions to it from the electric and magnetic dipole modes, Q^e_{scat} and Q^m_{scat}, respectively, for a three layer spherical nanoparticle. The external radius is $r_3 = 120$ nm. The outer Si layer is passive with $\kappa_2 = 0$. The concentric internal Ag layer has a central radius $r_c = 74.5$ nm and a thickness $t = 15$ nm. The inner Si layer is active. Different gain values ranging from $\kappa_1 = 0$ to $\kappa_1 = 0.5$ are considered.

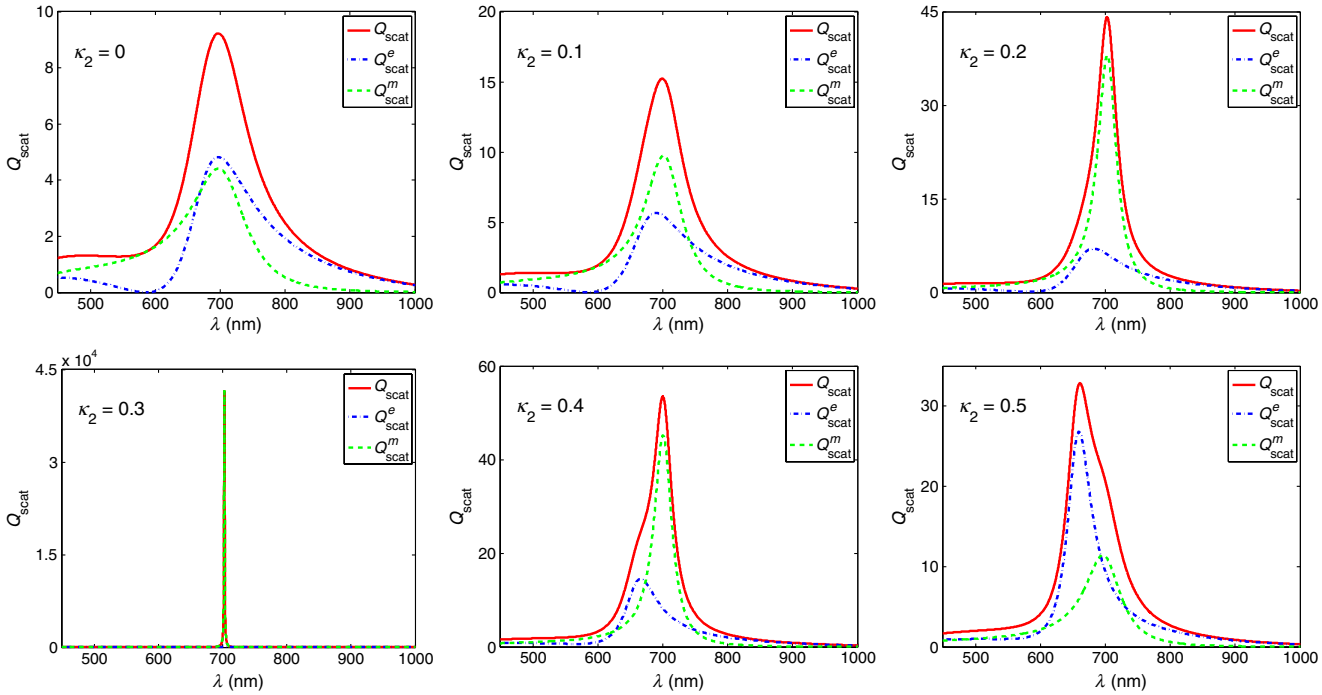

FIG. 10. Scattering efficiencies Q_{scat} and the contributions to it from the electric and magnetic dipole modes, Q^e_{scat} and Q^m_{scat}, respectively, for a three layer spherical nanoparticle. The external radius is $r_3 = 120$ nm. The inner Si layer is passive with $\kappa_1 = 0$. The concentric internal Ag layer has a central radius $r_c = 74.5$ nm and a thickness $t = 15$ nm. The outer Si layer is active. Different gain values ranging from $\kappa_2 = 0$ to $\kappa_2 = 0.5$ are considered.

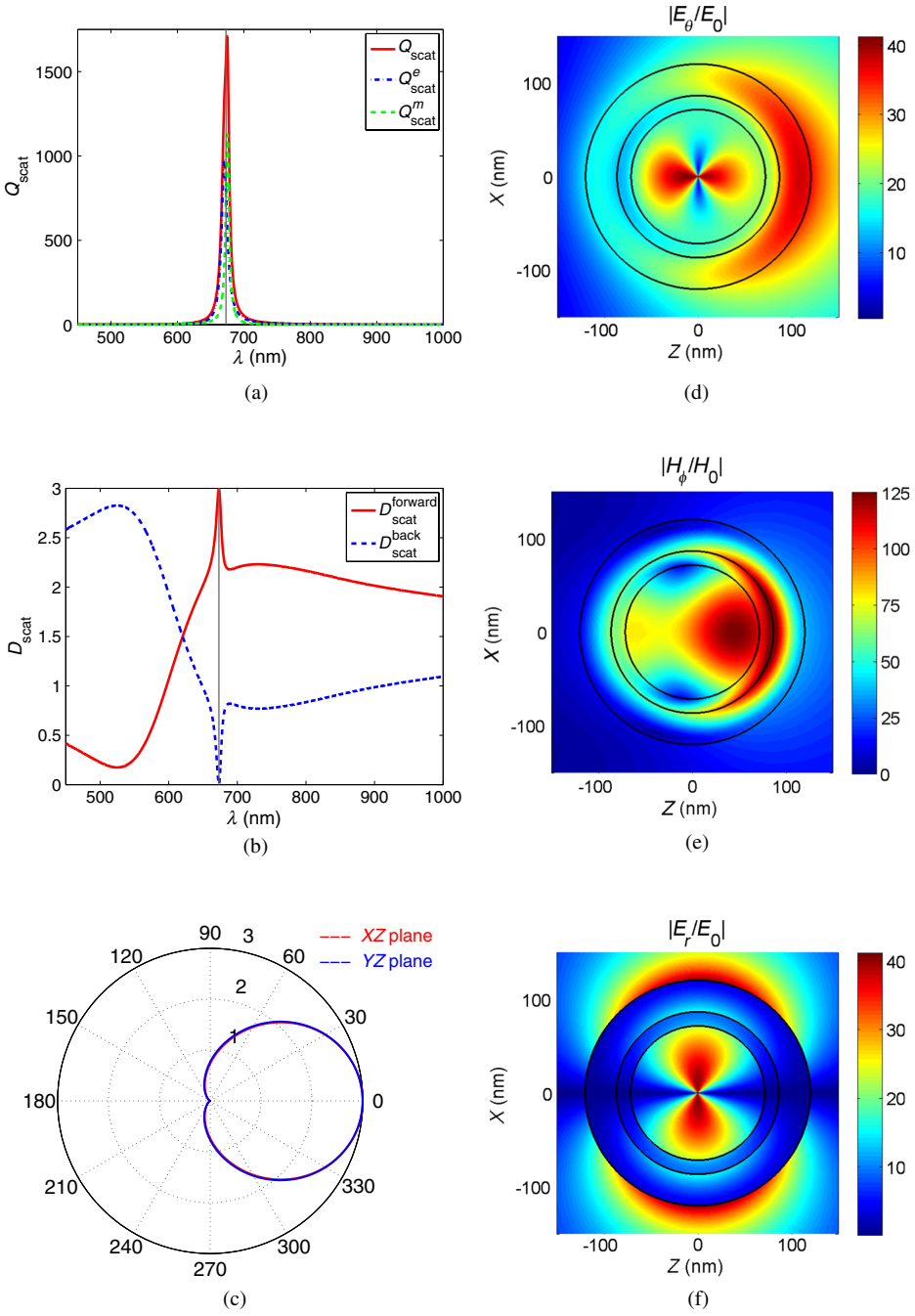

FIG. 11. (a) Scattering efficiency Q_{scat} and the contributions to it from the electric and magnetic dipole modes, Q^e_{scat} and Q^m_{scat}, respectively, for the active Huygens source nanoparticle. (b) Scattering directivity in the forward ($+\hat{\mathbf{z}}$) and backward ($-\hat{\mathbf{z}}$) directions. (c) Scattering directivity patterns in the XZ and YZ planes at the mode-balance wavelength $\lambda = 673.1$ nm. (d)–(f) Color maps of the magnitudes of the (d) E_θ, (e) H_ϕ, and (f) E_r field components, normalized by the incident field amplitude, on the XZ plane.

then varied to study the properties of the resonances and the associated responses. Note that Fig. 9 thus reveals that the electric dipole superresonance is excited at a threshold value of $\kappa_1 \simeq 0.4$.

Inversely, increasing the gain in the outer Si layer mostly benefits the TE^{o11} (magnetic dipole) resonance. This intuition is confirmed in Fig. 10, which represents the scattering efficiency Q_{scat} and the contributions to it from the electric and magnetic dipole modes, Q^e_{scat} and Q^m_{scat}, respectively, as the gain, κ_2, in the outer Si layer is increased. In this case, the inner Si layer is taken to be passive with $\kappa_1 = 0$. These results reveal that the magnetic dipole superresonance is excited at a threshold value of $\kappa_2 \simeq 0.3$.

As expected, the presence of gain also produces small shifts in the resonant frequencies. This arises from the fact that the gain constant κ affects both the real and imaginary parts of the permittivity of Si: $\varepsilon_{\text{Si}} = n^2_{\text{Si}} - \kappa^2 + j2n_{\text{Si}}\kappa$. However, since both resonances can be retuned by modifying the size and position of the plasmonic layer, one can follow an iterative procedure (increasing gain → retuning → increasing gain → retuning…) until the electric and magnetic dipole superresonances coincide. The net result is a Huygens particle that combines a huge Q_{scat} with

a maximal directivity $D_{\mathrm{scat}} = 3$. This iterative procedure is followed until $Q_{\mathrm{scat}} \sim 1500$ is obtained at the wavelength when $D_{\mathrm{scat}} = 3$. This value is obtained for the parameters $r_c = 79$ nm, $t = 15$ nm, $r_3 = 120$ nm, $\kappa_1 = 0.385$, and $\kappa_2 = 0.255$. Since, in theory, the scattering efficiency is unbounded for this canonical problem, the iterative optimization procedure could have continued, generating even larger scattering efficiencies. In practice, however, it will be limited by fabrication tolerances, bandwidth limitations, saturation of the gain media and other nonlinear effects.

A description of the performance of the active Huygens source nanoparticle is gathered in Fig. 11. Figure 11(a) depicts the scattering efficiency Q_{scat} and the contributions to it from the electric and magnetic dipole modes, Q^e_{scat} and Q^m_{scat}, respectively. It reveals that both the electric and magnetic dipole superresonances are balanced at a particular wavelength. Figure 11(b) next depicts the directivity D_{scat} in the forward ($+\hat{\mathbf{z}}$) and backward ($-\hat{\mathbf{z}}$) directions as a function of the wavelength. It illustrates that the maximum forward scattering directivity $D_{\mathrm{scat}} = 3$ (indicated by a solid gray line) is achieved at $\lambda = 673.1$ nm when both the electric and magnetic dipole responses are balanced. This is, of course, accompanied by the very large scattering efficiency $Q_{\mathrm{scat}} \sim 1500$ shown in Fig. 11(a). Figure 11(c) then presents the scattering directivity patterns in the XY and YZ planes at the mode-balance wavelength, i.e., $\lambda = 673.1$ nm. These results verify the Huygens source characteristics of the radiated fields. Finally, Figs. 11(d)–11(f) present color maps of the magnitudes of the electric and magnetic field components, normalized by the incident field amplitude, in the XZ plane at the mode-balance wavelength. The total fields, including both the TM^{e1n} and TE^{o1n} modes up to the multipole order $n_{\max} = 10$, reveal that the enhanced directivity is accompanied by a concentration of the tangential fields in the forward direction.

To finalize the discussion of the Huygens source nanoparticle laser, we note that while a dispersionless refractive index is assumed for the gain layers, the presented methodology enabled tuning both the electric and magnetic dipole resonances to a frequency of interest. The dispersion engineering problem would be solved in the same manner. The goal would be to have both the electric and magnetic resonances occur at the peak value of the dispersive gain model employed, respectively, in the appropriate gain-impregnated dielectric region. Moreover, as speculated and seen experimentally [35,74–77] and as demonstrated theoretically [48,78], the physical, bulk gain constants needed for the physical realization of gain-assisted nanostructures that exhibit extreme localization of the exciting fields in their gain regions and corresponding resonance-enhanced scattering cross sections are related to the effective values predicted directly from simulation, but are considerably less in reality because of those effects. The revised theoretical values, taking into account the impact of this resonant localization on the actual gain constants, are well within known values achieved by dyes [35], nanolasers [43], and quantum dots [79].

VII. CONCLUSIONS

An advanced design formulation for the investigation of resonant nanoparticles is introduced. This methodology is based on the induction theorem and associated radio frequency antenna engineering concepts. It consists of transforming the nanoscattering problem into a nanoradiating system, and then applying basic antenna theory design principles. In particular, the suppression of the total reactive power is used to design resonant nanoparticles and to understand the underlying physics associated with their resonances. This design process more closely aligns the study of nanoantennas with actual antenna concepts rather than scattering ones.

The standard analytical formalism associated with defining the radiated and reactive powers in spherical configurations itself is extended to include lossy (and gain) media. Although the required formulation is derived here to study analytically the scattering from multilayered, passive and active, spherical nanoparticles, the same process can be followed to treat arbitrary complex geometries with numerical simulators. It is validated by considering various well-known canonical configurations. To illustrate its potential, the capabilities of this mathematical apparatus and the induction theorem-based methodology are engaged to combine plasmonic and high-ε resonances in a three-layer concentric nanosphere. It is demonstrated that the methodology enables independent control over the electric and magnetic resonances, facilitating their superposition and frequency ordering exchange. This example also clearly emphasized how the approach provides additional physical insights into when and where resonances occur, and how several different resonance phenomena can be combined in a simple manner.

The efficacy of the methodology is proved by engineering the pathfinder design of a Huygens source nanoparticle laser. This nanoparticle laser combines a giant scattering efficiency with high directivity and zero backscattering. In particular, it represents the maximum directivity achievable with the combination of elementary electric and magnetic dipole modes, a limit usually considered as the *de facto* standard for subwavelength particles. Moreover, this nanoparticle laser exhibits isotropic behavior in the sense that it provides directional scattering into the direction of propagation of the incident field, independent of what that direction is.

We emphasize that the induction theorem-based methodology can be applied to a large number of resonant phenomena and nanoparticles. For example, although this work is focused on the electric and magnetic dipole resonances, which are the natural choice when dealing with subwavelength bodies, the same methodology can be

adapted to higher order resonances. Additionally, bearing in mind that scattering cancellation effects take place at the antiresonances of the particle, which in pairwise fashion accompany the resonances discussed in this article, the application of the induction theorem-based methodology may also be of great use in the design of cloaked nanoparticles. Furthermore, our results may be extended by combining the present analysis with more advanced antenna engineering techniques, in which the performance characteristics such as quality factor, bandwidth, bandwidth gain product, and/or radiation efficiency could be directly translated to the design of resonant nanoparticles. Consequently, we believe that the concepts introduced in this article may have a dramatic impact since they may open and stimulate new paradigms in the design and fundamental study of resonant nanoparticles and nanoantennas.

ACKNOWLEDGMENTS

This work was supported in part by the Spanish Ministry of Science and Innovation, Projects No. TEC2009-11995 and No. CSD2008-00066, and by the NSF Contract No. ECCS-1126572.

[1] C. F. Bohren and D. R. Huffman, *Absorption and Scattering of Light by Small Particles* (John Wiley & Sons, Hoboken, NJ, 1983).

[2] N. Engheta and R. W. Ziolkowski, *Metamaterials: Physics and Engineering Explorations* (IEEE Press-John Wiley & Sons, Hoboken, NJ, 2006).

[3] N. Engheta, Circuits with light at nanoscales: Optical nanocircuits inspired by metamaterials, Science **317**, 1698 (2007).

[4] M. E. Stewart, C. R. Anderton, L. B. Thompson, J. Maria, S. K. Gray, J. A. Rogers, and R. G. Nuzzo, Nanostructured plasmonic sensors, Chem. Rev. **108**, 494 (2008).

[5] I. Choi and Y. Choi, Plasmonic nanosensors: Review and prospect, IEEE J. Sel. Top. Quantum Electron. **18**, 1110 (2012).

[6] S. D. Campbell and R. W. Ziolkowski, Simultaneous excitation of electric and magnetic dipole modes in a resonant core-shell particle at infrared frequencies to achieve minimal backscattering, IEEE J. Sel. Top. Quantum Electron. **19**, 4700209 (2013).

[7] H. A. Atwater and A. Polman, Plasmonics for improved photovoltaic devices, Nat. Mater. **9**, 205 (2010).

[8] L. Novotny and N. van Hulst, Antennas for light, Nat. Photonics **5**, 83 (2011).

[9] P. Biagioni, J.-S. Huang, and B. Hecht, Nanoantennas for visible and infrared radiation, Rep. Prog. Phys. **75**, 024402 (2012).

[10] M. Agio, Optical antennas as nanoscale resonators, Nanoscale **4**, 692 (2012).

[11] L. Novotny and B. Hecht, *Principles of Nano-Optics* (Cambridge University Press, Cambridge, U.K., 2012), 2nd ed.

[12] A. Alù and N. Engheta, Theory, modeling and features of optical nanoantennas, IEEE Trans. Antennas Propag. **61**, 1508 (2013).

[13] M. Agio and A. Alù, *Optical Antennas* (Cambridge University Press, New York, 2013).

[14] R. W. Ziolkowski and A. D. Kipple, Reciprocity between the effects of resonant scattering and enhanced radiated power by electrically small antennas in the presence of nested metamaterial shells, Phys. Rev. E **72**, 036602 (2005).

[15] A. Alù and N. Engheta, Polarizabilities and effective parameters for collections of spherical nanoparticles formed by pairs of concentric double-negative, single-negative, and/or double-positive metamaterial layers, J. Appl. Phys. **97**, 094310 (2005).

[16] L. R. Hirsch, A. M. Gobin, A. R. Lowery, F. Tam, R. A. Drezek, N. J. Halas, and J. L. West, Metal nanoshells, Ann. Biomed. Eng. **34**, 15 (2006).

[17] S. Arslanagić, R. W. Ziolkowski, and O. Breinbjerg, Analytical and numerical investigation of the radiation from concentric metamaterial spheres excited by an electric Hertzian dipole, Radio Sci. **42**, RS6S16 (2007).

[18] N. J. Halas, Plasmonics: An emerging field fostered by nano letters, Nano Lett. **10**, 3816 (2010).

[19] A. Alù and N. Engheta, Achieving transparency with plasmonic and metamaterial coatings, Phys. Rev. E **72**, 016623 (2005).

[20] A. Alù and N. Engheta, Plasmonic and metamaterial cloaking: Physical mechanisms and potentials, J. Opt. A **10**, 093002 (2008).

[21] S. Arslanagić and R. W. Ziolkowski, Active coated nanoparticle excited by an arbitrarily located Hertzian dipole—resonance and transparency effects, J. Opt. **12**, 024014 (2010).

[22] F. Monticone and A. Alù, Do cloaked objects really scatter less?, Phys. Rev. X **3**, 041005 (2013).

[23] S. Arslanagić and R. W Ziolkowski, Jamming of quantum emitters by active coated nanoparticles, IEEE J. Sel. Top. Quantum Electron. **19**, 4800506 (2013).

[24] K. Berdel, J. G. Rivas, P. H. Bolivar, P. de Maagt, and H. Kurz, Temperature dependence of the permittivity and loss tangent of high-permittivity materials at terahertz frequencies, IEEE Trans. Microwave Theory Tech. **53**, 1266 (2005).

[25] M. J. Weber, *Handbook of Optical Materials* (CRC Press, Boca Raton, FL, 2003).

[26] H. H. Li, Refractive index of silicon and germanium and its wavelength and temperature derivatives, J. Phys. Chem. Ref. Data **9**, 561 (1980).

[27] A. I. Kuznetsov, A. E. Miroshnichenko, Y. H. Fu, J. B. Zhang, and B. Lukyanchuk, Magnetic light, Sci. Rep. **2**, 492 (2012).

[28] A. B. Evlyukhin, S. M. Novikov, U. Zywietz, R. L. Eriksen, C. Reinhardt, S. I. Bozhevolnyi, and B. N. Chichkov, Demonstration of magnetic dipole resonances of dielectric nanospheres in the visible region, Nano Lett. **12**, 3749 (2012).

[29] F. Shafiei, F. Monticone, K. Q. Le, X.-X. Liu, T. Hartseld, A. Alù, and X. Li, A subwavelength plasmonic metamolecule exhibiting magnetic-based optical fano resonance, Nat. Nanotechnol. **8**, 95 (2013).

[30] Y. H. Fu, A. I. Kuznetsov, A. E. Miroshnichenko, Y. F. Yu, and B. Lukyanchuk, Directional visible light scattering by silicon nanoparticles, Nat. Commun. **4**, 1527 (2013).
[31] S. Person, M. Jain, Z. Lapin, J. J. Sáenz, G. Wicks, and L. Novotny, Demonstration of zero optical backscattering from single nanoparticles, Nano Lett. **13**, 1806 (2013).
[32] M. Kerker, D. S. Wang, and C. L. Giles, Electromagnetic scattering by magnetic spheres, J. Opt. Soc. Am. **73**, 765 (1983).
[33] M. Kerker, Resonances in electromagnetic scattering by objects with negative absorption, Appl. Opt. **18**, 1180 (1979).
[34] J. A. Gordon and R. W. Ziolkowski, The design and simulated performance of a coated nano-particle laser, Opt. Express **15**, 2622 (2007).
[35] M. A. Noginov, G. Zhu, A. M. Belgrave, Reuben Bakker, V. M. Shalaev, E. E. Narimanov, S. Stout, E. Herz, T. Suteewong, and U. Wiesner, Demonstration of a spaser-based nanolaser, Nature (London) **460**, 1110 (2009).
[36] A. De Luca, M. P. Grzelczak, I. Pastoriza-Santos, L. M. Liz-Marzan, M. La Deda, M. Striccoli, and G. Strangi, Dispersed and encapsulated gain medium in plasmonic nanoparticles: A multipronged approach to mitigate optical losses, ACS Nano **5**, 5823 (2011).
[37] M. Klopfer and R. K. Jain, Plasmonic quantum dots for nonlinear optical applications [invited], Opt. Mater. Express **1**, 1353 (2011).
[38] S. Campione, M. Albani, and F. Capolino, Complex modes and near-zero permittivity in 3D arrays of plasmonic nanoshells: Loss compensation using gain, Opt. Mater. Express **1**, 1077 (2011).
[39] J. Pan, Z. Chen, J. Chen, P. Zhan, C. J. Tang, and Z. L. Wang, Low-threshold plasmonic lasing based on high-q dipole void mode in a metallic nanoshell, Opt. Lett. **37**, 1181 (2012).
[40] I. Liberal, I. Ederra, R. Gonzalo, and R. W. Ziolkowski, Magnetic dipole super-resonances and their implications in optical forces, Opt. Express **22**, 8640 (2014).
[41] I. E. Protsenko, A. V. Uskov, O. A. Zaimidoroga, V. N. Samoilov, and E. P. O'Reilly, Dipole nanolaser, Phys. Rev. A **71**, 063812 (2005).
[42] A. K. Sarychev and G. Tartakovsky, Magnetic plasmonic metamaterials in actively pumped host medium and plasmonic nanolaser, Phys. Rev. B **75**, 085436 (2007).
[43] M. T. Hill, Status and prospects for metallic and plasmonic nano-lasers [invited], J. Opt. Soc. Am. B **27**, B36 (2010).
[44] J. Geng, R. W. Ziolkowski, R. Jin, and X. Liang, Numerical study of the near-field and far-field properties of active open cylindrical coated nanoparticle antennas, IEEE Photon. **3**, 1093 (2011).
[45] K. Ding and C. Z. Ning, Metallic subwavelength-cavity semiconductor nanolasers, Light Sci. Appl. **1**, e20 (2012).
[46] M. Khajavikhan, A. Simic, M. Katz, J. H. Lee, B. Slutsky, A. Mizrahi, V. Lomakin, and Y. Fainman, Thresholdless nanoscale coaxial lasers, Nature (London) **482**, 204 (2012).
[47] Y.-J. Lu, J. Kim, H.-Y. Chen, C. Wu, N. Dabidian, C. E. Sanders, C.-Y. Wang, M.-Y. Lu, B.-H. Li, X. Qiu, W.-H. Chang, L.-J. Chen, G. Shvets, C.-K. Shih, and S. Gwo, Plasmonic nanolaser using epitaxially grown silver film, Science **337**, 450 (2012).
[48] S. D. Campbell and R. W. Ziolkowski, Impact of strong localization of the incident power density on the nano-amplifier characteristics of active coated nano-particles, Opt. Commun. **285**, 3341 (2012).
[49] D. A. Miller, On perfect cloaking, Opt. Express **14**, 12457 (2006).
[50] M. Selvanayagam and G. V. Eleftheriades, Experimental demonstration of active electromagnetic cloaking, Phys. Rev. X **3**, 041011 (2013).
[51] A. Alù and N. Engheta, Enhanced directivity from sub-wavelength infrared/optical nano-antennas loaded with plasmonic materials or metamaterials, IEEE Trans. Antennas Propag. **55**, 3027 (2007).
[52] A. Alù and N. Engheta, Higher-order resonant power flow inside and around superdirective plasmonic nanoparticles, J. Opt. Soc. Am. B **24**, A89 (2007).
[53] Z. Ruan and S. Fan, Superscattering of light from sub-wavelength nanostructures, Phys. Rev. Lett. **105**, 013901 (2010).
[54] Z. Ruan and S. Fan, Design of subwavelength superscattering nanospheres, Appl. Phys. Lett. **98**, 043101 (2011).
[55] W. Liu, A. E. Miroshnichenko, D. N. Neshev, and Y. S. Kivshar, Broadband unidirectional scattering by magneto-electric core-shell nanoparticles, ACS Nano **6**, 5489 (2012).
[56] X. Meng, U. Guler, A. V. Kildishev, K. Fujita, K. Tanaka, and V. M. Shalaev, Unidirectional spaser in symmetry-broken plasmonic core-shell nanocavity, Sci. Rep. **3**, 1241 (2013).
[57] C. A. Balanis, *Antenna Theory: Analysis and Design* (John Wiley & Sons, New York, 2012), 3rd ed.
[58] R. F. Harrington, *Time-Harmonic Electromagnetic Fields* (McGraw-Hill, Inc., New York, 1961).
[59] C. A. Balanis, *Advanced Engineering Electromagnetics* (Wiley New York, New York, 2012), 2nd ed.
[60] See Supplemental Material at http://link.aps.org/supplemental/10.1103/PhysRevApplied.1.044002 for a detailed derivation of the analytical formalism introduced in Sec. III, as well as the analysis of several canonical resonant nanoparticle configurations using the induction theorem methodology.
[61] R. W. Ziolkowski and A. D. Kipple, Application of double negative materials to increase the power radiated by electrically small antennas, IEEE Trans. Antennas Propag. **51**, 2626 (2003).
[62] J. L. Volakis, C.-C. Chen, and K. Fujimoto, *Small Antennas: Miniaturization Techniques & Applications* (McGraw-Hill, New York, 2010).
[63] R. W. Ziolkowski, P. Jin, and C.-C. Lin, Metamaterial-inspired engineering of antennas, Proc. IEEE **99**, 1720 (2011).
[64] R. E. Collin, *Field Theory of Guided Waves* (IEEE Press, New York, 1991), 2nd ed.
[65] A. D. Yaghjian and S. R. Best, Impedance, bandwidth, and Q of antennas, IEEE Trans. Antennas Propag. **53**, 1298 (2005).
[66] L. D. Landau and E. M. Lifshitz, *Electrodynamics of Continuous Media* (Pergamon Press, New York, 1960).
[67] S. R. Best, The foster reactance theorem and quality factor for antennas, IEEE Antennas Wireless Propag. Lett. **3**, 306 (2004).

[68] N. Engheta, Is foster's reactance theorem satisfied in double-negative and single-negative media?, Microwave Opt. Technol. Lett. **39**, 11 (2003).

[69] T. V. Hansen, O. S. Kim, and O. Breinbjerg, Stored energy and quality factor of spherical wave functions in relation to spherical antennas with material cores, IEEE Trans. Antennas Propag. **60**, 1281 (2012).

[70] I. Liberal, I. Ederra, R. Gonzalo, and R. W. Ziolkowski, A multipolar analysis of near-field absorption and scattering processes, IEEE Trans. Antennas Propag. **61**, 5184 (2013).

[71] Feshbach Morse, *Methods of Theoretical Physics* (McGraw-Hill, Inc., New York, 1981), Pt. II.

[72] I. Liberal and R. W. Ziolkowski, Analytical and equivalent circuit models to elucidate power balance in scattering problems, IEEE Trans. Antennas Propag. **61**, 2714 (2013).

[73] N. Engheta, A. Salandrino, and A. Alù, Circuit elements at optical frequencies: Nanoinductors, nanocapacitors, and nanoresistors, Phys. Rev. Lett. **95**, 095504 (2005).

[74] M. A. Noginov, G. Zhu, V. P. Drachev, and V. M. Shalaev, Surface plasmons and gain media, in *Nanophotonics with Surface Plasmons* (Elsevier, Amsterdam, 2007) Chap. 5, pp. 141–169.

[75] Y. Sivan, S. Xiao, U. K. Chettiar, A. V. Kildishev, and V. M. Shalaev, Frequency-domain simulations of a negative-index material with embedded gain, Opt. Express **17**, 24060 (2009).

[76] A. Fang, T. Koschny, and C. M. Soukoulis, Lasing in metamaterial nanostructures, J. Opt. **12**, 024013 (2010).

[77] S. Xiao, V. P. Drachev, A. V. Kildishev, X. Ni, U. K. Chettiar, H.-K.n Yuan, and V. M. Shalaev, Loss-free and active optical negative-index metamaterials, Nature (London) **466**, 735 (2010).

[78] D. B. Li and C. Z. Ning, Giant modal gain, amplified surface plasmon-polariton propagation, and slowing down of energy velocity in a metal-semiconductor-metal structure, Phys. Rev. B **80**, 153304 (2009).

[79] S. D. Campbell and R. W. Ziolkowski, The performance of active coated nanoparticles based on quantum-dot gain media, Adv. OptoElectron. **2012**, 368786 (2012).